RSC Advances

ROYAL SOCIETY OF CHEMISTRY

PAPER

View Article Online
View Journal | View Issue

Check for updates

Cite this: *RSC Adv.*, 2020, **10**, 34859

Facile construction of Fe, N and P co-doped carbon spheres by carbothermal strategy for the adsorption and reduction of U(VI)†

Zhimin Dong,[a] Zhibin Zhang,*[a] Runze Zhou,[a] Yayu Dong,[b] Yuanyuan Wei,[a] Zhijian Zheng,[a] Youqun Wang,[a] Ying Dai,[a] Xiaohong Cao[a] and Yunhai Liu *[a]

Received 18th July 2020
Accepted 17th August 2020

DOI: 10.1039/d0ra06252a

rsc.li/rsc-advances

In this work, nitrogen and phosphorus co-doped magnetic carbon spheres encapsulating well-dispersed active Fe nanocrystals (Fe/P-CN) were fabricated *via* a simple copolymer pyrolysis strategy. Benefiting from heteroatoms doping, Fe/P-CN could primarily adsorb soluble U(VI) ions through abundant functional groups, and subsequently, the adsorbed U(VI) could be reduced to insoluble U(IV) by Fe nanocrystals. Fe/P-CN pyrolyzed at 800 °C (Fe/P-CN-800) exhibited excellent U(VI) removal capacity of 306.76 mg g^{-1}, surpassing nitrogen and phosphorus co-doped carbon spheres and nano zero-valent iron. In addition, the magnetic separation and thermal reactivation properties endow Fe/P-CN-800 with excellent reusability. This research, especially, provides a promising synergistic adsorption and reduction strategy to effectively remove U(VI) using heteroatom-doped composites.

Introduction

With the development of nuclear energy, nuclear waste containing radionuclides is inevitably discharged into environment, leading to serious environmental contamination issues. Uranium, especially, is considered a serious threat to the ecological environment and human health due to its inherent nature of being highly hydrophilic, immobile and has a long half-life. Therefore, safe and effective methods for the disposal of radioactive waste have attracted intense research interest worldwide.[1–5] Among the various strategies for environmental remediation, adsorption has proved to be an effective method for removing U(VI) and other radionuclides because of its low cost, extensive adaptability, and environmental friendliness.[6,7] Besides, the reductive immobilization of U(VI) to insoluble U(IV) is also a simple and efficient method to separate U(VI) from wastewater.[8,9] Hence, exploring the dual feasibility of adsorbing and reducing U(VI) to eliminate chemical toxicity and radiotoxicity is imperative.

As an ideal candidate, nano zero-valent iron (NZVI) can reduce U(VI) to insoluble U(IV) effectively, and the reductive immobilization and adsorption of U(VI) can occur on the surface of NZVI, which is mainly due to robust Van der Waals, magnetic attractive forces and abundant active sites.[10] Therefore, the mobility of U(VI) is restrained and deposited on the surface of iron corrosive products.[11,12] However, many practical results demonstrate that the performance of NZVI may be restricted by its rapid aggregation and deactivation on account of its intrinsic magnetic interactions and high surface energy.[13]

Thus, to improve the dispersity and stability of NZVI, various methods have been investigated, such as surface modification,[14–16] and inorganic clay mineral[17–19] and porous support materials.[20,21] Among them, heteroatom-doped porous carbon matrices are the known ideal candidates to distribute NZVI uniformly, and can inherit the unconventional advantages of building blocks and acquire exceptional properties simultaneously.[22] For example, Kairuo *et al.*[23] reported that N-doped carbon nanospheres embedded with Fe nanocrystals could offer extra active sites for binding uranyl ions and enhance the electrostatic driving force between the adsorbent and U(VI). More importantly, Fe nanocrystals were crucial for reducing U(VI). Interestingly, compared with single heteroatom doping, heteroatoms co-doping could achieve more colossal asymmetric spin and charge density due to the synergy of heteroatoms.[24,25] Consequently, nitrogen and phosphorus heteroatoms doped carbon, which form phosphorus bridges (P–C and P–O) and nitrogen bridges (C–N, C=N, and N–O) can enhance the metal ion adsorption capacity and selectivity.[26] Accordingly, N,P co-doped porous carbon will be an effective matrix to embed Fe nanocrystals and achieve multiple properties including adsorption, reduction and magnetic separation. However, despite their anticipated potential, heteroatom co-doped

---

[a] State Key Laboratory of Nuclear Resources and Environment, East China University of Technology, Nanchang, Jiangxi 330013, P. R. China. E-mail: Walton_liu@163.com; zhbzhang@ecut.edu.cn

[b] MIIT Key Laboratory of Critical Materials Technology for New Energy Conversion and Storage, School of Chemistry and Chemical Engineering, Harbin Institute of Technology, Harbin 150001, P. R. China

† Electronic supplementary information (ESI) available. See DOI: 10.1039/d0ra06252a

carbon spheres have seldomly been employed for removing U(VI).

Herein, we fabricate magnetic carbon spheres (Fe/P-CN-*X*, *X* is the temperature of copolymer pyrolysis) co-doped with heteroatoms (N, P and Fe^0) *via* a simple copolymer pyrolysis strategy. The as-synthesized nanospheres were characterized *via* SEM, TEM, XRD, TG and N_2 adsorption–desorption in detail. Additionally, their removal performance of U(VI) was systematically studied *via* batch experiments. Furthermore, the adsorption and reduction coaction mechanism were also investigated.

Experimental

Preparation of Fe, N and P co-doped carbon spheres

The preparation process of the Fe, N and P co-doped carbon spheres is schematically shown in Scheme 1. Polyacrylonitrile was synthesized according to a modified method.[27,28] Typically, 6.20 mL acrylonitrile was dissolved in 95 mL water, and 0.10 g potassium persulfate and 1.00 g sodium dodecyl sulfate were added and then stirred at 70 °C for 12 h under the protection of N_2. Afterwards, the as-prepared product was soaked in a solution of $FeCl_3 \cdot 6H_2O$ and $(NH_4)_2HPO_4$ ($PAN : FeCl_3 \cdot 6H_2O : (NH_4)_2HPO_4 = 1 : 0.50 : 0.50$ (weight ratio)) and stirred for 24 h. The Fe/P-CN precursors were obtained by centrifugation, then washed with water and freeze-dried for 24 h. Finally, for Fe/P-CN-*X*, the precursors were calcined at a slow heating rate of 0.1 °C min^{-1} up to 300 °C in air for oxidation and then 1.5 °C min^{-1} to 600–900 °C for 2 h under N_2. As a control, P-CN without Fe doping and pristine CN were prepared using the same procedures.

Results and discussion

Characterization of Fe/P-CN-*X*

Fig. 1a shows the XRD patterns of the samples, where the peaks at 13.6° (100) and 42.2° (100) are attributed to the in-plane repetitive units of the continuous heptazine framework and the stacking of the graphitic crystal plane, respectively.[29] In comparison with the characteristic peak (002) of graphitic carbon nitride (g-CN) at 27°, this peak shifts to 31.9° for Fe/P-CN-*X*, indicating that the interplanar distance decreases after doping with P and Fe.[30] Additionally, the peaks at 19°, 24° and 35.4° demonstrate the presence of Fe_3O_4 (JCPDS No 88-315, ☆) in Fe/P-CN-600 and Fe/P-CN-700.

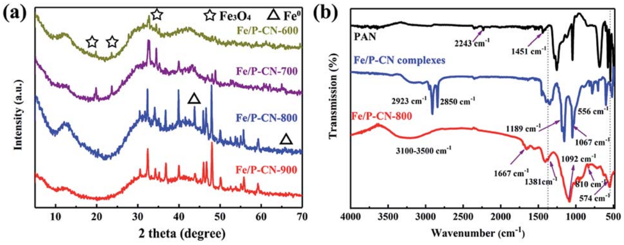

Fig. 1 (a) XRD patterns of Fe/P-CN-*X* and (b) FT-IR spectra of PAN, Fe/P-CN precursors, and Fe/P-CN-800.

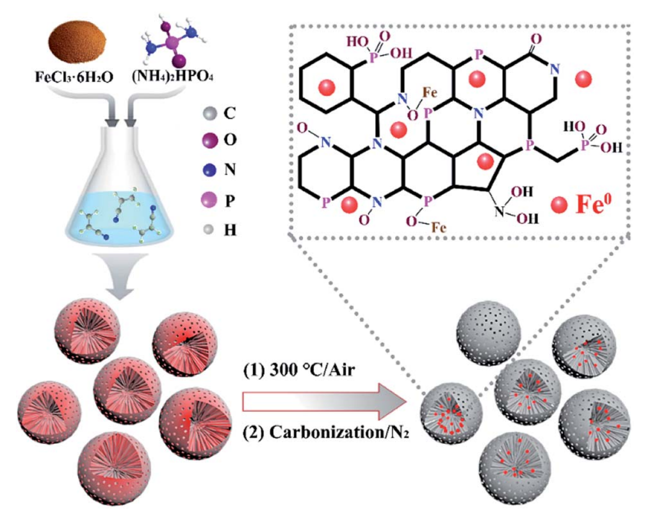

Scheme 1 Process for the synthesis of Fe, N and P co-doped carbon spheres.

However, the peaks of Fe_3O_4 disappear for Fe/P-CN-800 and Fe/P-CN-900, and new peaks at 44.8° and 65.2° corresponding to the (110) and (200) facets of α-Fe emerge, respectively (PDF No. 87-0722, △). Therefore, the Fe^{3+} species is transformed to F_3O_4, which is further reduced to metallic iron and Fe_3C phase by the carbon in the N_2 atmosphere during the pyrolysis process. Considering the peak intensity of iron, 800 °C was selected as the most suitable calcination temperature for Fe/P-CN-*X* since in resulted in more metallic Fe.

The distinct type IV isotherms with an obvious hysteresis loop in the N_2 adsorption–desorption isotherms (Fig. S1a†) indicate the existence of a porous structure.[31] Also, the pore size distribution obtained from the N_2 adsorption experiments (Fig. S1b†) confirms the presence of mesopores. The pore size distribution was determined using the Barrett–Joyner–Halenda (BJH) method, which demonstrates that the size of the mesopores of Fe/P-CN-*X* is mainly less than 20 nm. Additionally, the BET specific surface area (S_{BET}) of Fe/P-CN-600, Fe/P-CN-700, Fe/P-CN-800 and Fe/P-CN-900 were calculated to be 39.81, 99.32, 234.02 and 334.36 $m^2\ g^{-1}$, the total pore volume (V_t) 0.13, 0.19, 0.24 and 0.25 $cm^3\ g^{-1}$, and the average pore diameter (D_A) 10.87, 12.87, 12.97 and 13.07 nm (Table S1†), respectively. The porous structure and high surface area of Fe/P-CN-*X* endow it with sufficiently exposed active sites for adsorbing U(VI). Although the S_{BET} of Fe/P-CN-900 is the largest, the higher proportion of metallic Fe indicates that Fe/P-CN-800 is more suitable for reducing U(VI).

As shown in Fig. 1b, the typical absorption peaks appeared at 2243 cm^{-1} (C≡N) and 1451 cm^{-1} [$(CH_2)_n$],[32] confirming the successful fabrication of PAN. However, the absorption peak of C≡N disappeared from the Fe/P-CN precursors, and the stretching vibration of the $-CH_2-$ group was retained at 2923 and 2850 cm^{-1}, indicating that C≡N participates in the hydrolysis and grafting reactions. Surprisingly, two new peaks appeared at 1189 and 1067 cm^{-1}, which correspond to the vibration absorption of P═O and the stretch absorption of P–O in the phosphonate groups, respectively.[33] The new peak at 556 cm^{-1} is ascribed to the vibration absorption of Fe–O.[34] After pyrolysis, the peaks that emerged at 3100–3500, 1667, 1381 and 810 cm^{-1} in Fe/P-CN-800 are assigned to the characteristic absorption of N–H, O–H, C=N, and C–N in the triazine unit, respectively.[35] Meanwhile, the shift in the characteristic peaks of P=O and P–O to a broad peak at 1092 cm^{-1} corresponds to the combination of phosphorus-containing moieties, indicating that the phosphonate groups were retained after carbonization. Obviously, abundant active sites, such as phosphonate groups, nitrogen groups and metallic Fe moieties, are also present in Fe/P-CN-800, which can enhance its affinity for U(VI).

The SEM image shows that there are some discrete carbon spheres on the fluffy surface of Fe/P-CN-800. It should be noted that the spherical architectures were still maintained during the high temperature pyrolysis (Fig. 2a). The corresponding mapping images indicate that O, N, Fe, N and P elements are uniformly distributed throughout the carbon matrix. The well-defined spherical structures were also confirmed by TEM, as depicted in Fig. 2b. Many dark parts appeared in the body of the carbon spheres of Fe/P-CN-800, which can be interpreted as metal Fe nanoparticles uniformly embedded in the carbon spheres.

TG analysis was adopted to reveal the thermostability of Fe/P-CN-800 (Fig. 2c). The absorbed water was eliminated in the first stage (<200 °C). Then, the mass loss in the range of 200–370 °C can be attributed to the generation of α-Fe_2O_3 from Fe (Fe_3O_4 or Fe_3C) combined with the pyrolysis of labile oxygen-containing groups (amino and hydroxyl groups).[36] The final weight loss (<720 °C) is ascribed to the collapse of exposed carboxyl and phosphonate groups.[33] The stabilized weight after 720 °C indicates the total decomposition of the heteroatom co-doped carbon matrix and formation of Fe_2O_3 from iron compounds. Also, the final content of Fe_2O_3 is 42.56 wt%, with the proportion of elemental Fe of about 29.79 wt%, which is consistent with the energy dispersive X-ray spectroscopy (EDS) results (Fig. S2a†). Meanwhile, Fe/P-CN-800 exhibited favourable thermal stability, which is beneficial for the purification of radionuclide wastewater at an elevated temperature.

Influence of pH

The effects of pH on the removal of uranium by Fe/P-CN-600, Fe/P-CN-700, Fe/P-CN-800, and Fe/P-CN-900 were investigated in the initial pH range of 2.0–5.5. As shown in Fig. 3a, the removal capacity of the four samples increased dramatically in the pH range of 2.0 to 4.5, and then clearly decreased. At pH = 4.5, the maximum removal capacity of U(VI) achieved on Fe/P-CN-800 was 306.76 mg g^{-1}, which was higher than that of Fe/P-CN-600 (121.15 mg g^{-1}), Fe/N-C-700 (144.22 mg g^{-1}) and Fe/P-CN-900 (245.95 mg g^{-1}). The quantitative results of the P/N/Fe contents for these four samples were verified by the EDS (Fig. S2†), which could secondarily identify the main factors determining the removal capacity of U(VI). The results showed that the oxygen content decreased from 36.72% to 24.82% with an increase in the calcination temperature from 600 °C to 900 °C. Hence, there are two main reasons for achieving the maximum removal capacity of U(VI) on Fe/P-CN-800. Firstly, Fe/P-CN-800 possessed the maximum proportion of metallic Fe/Fe_3O_4 nanoparticles, which could reduce U(VI) to insoluble U(IV) effectively. Then, its other functional groups (such as pyridinic N) with a negative charge are beneficial for the reduction of U(VI). This means that the pyrolysis temperature can selectively regulate the removal capacity. Meanwhile, the surface charge of the material and distribution of uranium species primarily depend on the pH, resulting in a change in the U(VI) removal capacity.[34]

On the one hand, the relevant distribution of U(VI) species (50 mg L^{-1}) in aqueous solution was simulated using Visual MINTEQ.[23] U(VI) is mainly in the form of free uranyl (UO_2^{2+})

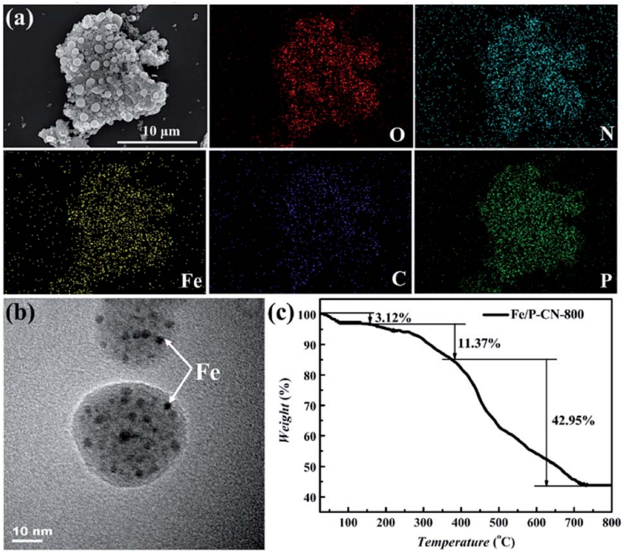

Fig. 2 (a) SEM image and the corresponding element mapping, (b) TEM image and (c) TG curve of Fe/P-CN-800.

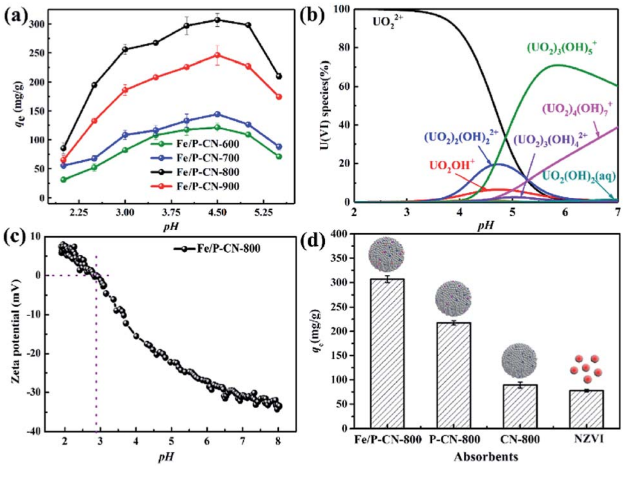

Fig. 3 (a) Effect of pH on the adsorption of U(VI) by Fe/P-CN-X (C_0 = 50 mg L^{-1}, m/V = 0.1 g L^{-1}, T = 298.15 K and t: 300 min). (b) Relative distribution of U(VI) species as a function of pH. (c) Zeta potential of Fe/P-CN-800. (d) Removal capacity of various absorbents (m/V = 0.1 g L^{-1}, pH = 4.5, C_0 = 50 mg L^{-1}, T = 298.15 K and t = 300 min).

between pH 2.0–4.0, and then slowly transforms into UO_2OH^+, $(UO_2)_2(OH)_2^{2+}$, $(UO_2)_3(OH)_5^+$, UO_2OH^+, $UO_2(OH)_2$ (aq) and $(UO_2)_4(OH)_7^+$ with an increase in pH from 4.0 to 7.0 (Fig. 3b). On the other hand, the surface charge value of Fe/P-CN-800 was also determined *via* a zeta potential test. The point of zero charge (pH_{pzc}) value of Fe/P-CN-800 is 2.87 (Fig. 3c), which is much lower than of Fe/N-C-700 of 4.60,[19] magnetic porous carbon of 6.80,[35] and DI-SNZVI of 6.41.[36] Benefiting from heteroatom doping, the pH_{pzc} value was reduced rapidly due to the donation of extra electrons.

Therefore, electrostatic repulsion should be responsible for the lower adsorption at pH < 2.87, where other positive ions, such as H^+ and Na^+, would compete with UO_2^{2+} for the adsorption sites.[37] When the pH increased from 2.87 to 4.50, the uptake amount of U(VI) species also increased because of the weakened protonation degree of the phosphonate groups and nitrogen groups and the negative surface charge of Fe/P-CN-800 ($pH > pH_{pzc}$), which could effectively attract the positively charged species of U(VI) electrostatically. Also, the reduction of U(VI) occurred simultaneously by the encapsulated Fe, leading to an increase in the removal capacity. Then, precipitated uranium species, such as $UO_2(OH)_2$(aq), would be generated at pH > 5.0. Therefore, the optimum pH value was set at 4.5 in the subsequent studies.

In addition, various absorbents (Fe/P-CN-800, P-CN-800, CN-800 and NVZI nanoparticles) were also prepared to compare the sequestration capacity. According to Fig. 3d, the uptake capacity of U(VI) on Fe/P-CN-800 (306.76 mg g^{-1}) is superior among the absorbents (that on P-CN-800, CN-800, and NVZI is 217.63, 89.21 and 77.63 mg g^{-1}, respectively), which can be ascribed to the heteroatom doping (including Fe, P, and N) effects. The doped heteroatoms provide a higher density of reactive sites and good electron-donating tendency, significantly enhancing the U(VI) removal capacity by generating strong surface complexation and chemisorption as well as redox interaction between Fe/P-CN-800 and U(VI).

Sorption kinetic

The adsorption rate is another crucial factor to evaluate the practical application of an adsorbent. As shown in Fig. 4a, the removal capacity of U(VI) on Fe/P-CN-800 increased rapidly to 40.85% in the initial 60 min, which is ascribed to its abundant active sites.[38] Then, U(VI) entered the internal region of Fe/P-CN-800, where there was a longer diffusion distance to bond with the inner free active sites. Thus, the removal capacity increased slowly,[39] and then remained constant at 300 min within the relative error.

The sorption kinetics of U(VI) on Fe/P-CN-800 was simulated with the pseudo-first-order,[40] pseudo-second-order,[41] and intraparticle diffusion models[42] (see ESI, S3†). According to eqn (S2)–(S4),† linear transformed models were employed to fit the kinetic data, as shown in Fig. 4a, b and S4.† According to Table S2,† the correlation coefficient value (R^2) from the pseudo-second-order kinetic model is 0.99, which is higher than that of the pseudo-first-order model (0.87), demonstrating that the primary removal U(VI) mechanism is chemisorption and the reduction reaction.[43] Meanwhile, the calculated q_e using the pseudo-second-order model is 310.54 mg g^{-1} and closer to the experimental data (306.76 mg g^{-1}). In addition, the whole removal process can be divided into three distinct limiting processes according to the three different slopes (Fig. 4b). Clearly, the higher k_{int} value in the first stage (Table S2†) indicated that intra-particle diffusion is the rate-limiting step because its removal rate is lower than film diffusion.[44] Meanwhile, the lines in the first and second stages do not pass through the origin, highlighting that diffusion and other reactions (such as electrostatic interaction and chemical redox) are simultaneously involved in the removal process.

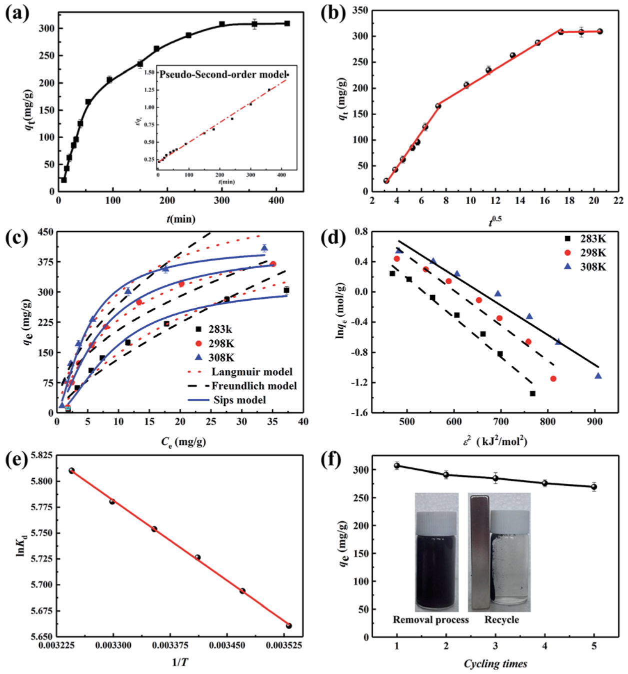

Fig. 4 (a and b) Sorption kinetics ($C_0 = 50$ mg L^{-1}, $m/V = 0.1$ g L^{-1}, $T = 298$ K and pH = 4.5) and fitted kinetic adsorption data using the pseudo-second order kinetic model is shown in the inset of (a) and (c and d) sorption isotherms of Fe/P-CN-800 ($t = 300$ min, $m/V = 0.1$ g L^{-1}, $T = 298$ K and pH = 4.5). (e) Liner plots of $\ln K_d$ *versus* $1/T$. (f) Recycle of Fe/P-CN-800. Inset shows images of the magnetic separation.

Adsorption isotherms and thermodynamic study

To evaluate the adsorption behaviour and thermodynamic properties of U(VI) on Fe/P-CN-800, its adsorption isotherms were measured at different temperatures (283.15, 298.15, and 308.15 K). Consequently, the enhanced sequestration capacities of Fe/P-CN-800 with an increase in temperature (Fig. 4c) show that high temperature is beneficial for the adsorption of U(VI). Additionally, four equilibrium isotherm models (*i.e.*, Langmuir, Sips, Freundlich, and Dubinin–Radushkevich) were utilized to non-linear fit the experimental data according to eqn (S5)–(S9)† (Fig. 4c), and the corresponding parameters are tabulated in Table S3.†[45]

According to Fig. 4c and Table S3,† the adsorption isotherms were better fitted by the Sips model ($R^2 = 0.98$) compared with the Langmuir model ($R^2 > 0.96$) and Freundlich model ($R^2 > 0.85$), which indicates that multilayer adsorption occurs at low concentration, while monolayer adsorption occurs at high concentration.[50] This can be explained as the synergistic adsorption (by affinity groups, *e.g.*, phosphonate groups, nitrogen groups and other oxygenated groups) and reduction process (adsorbed U(VI) reduced to insoluble U(IV) by NZVI). The maximum removal capacity obtained by the Sips model was 372.60 mg g^{-1}, which is dramatically higher than that of other reported NZVI-based absorbents (Table 1). Therefore, the synthesized Fe/P-CN-800 is a potential candidate to remove U(VI) from wastewater. The E_{DR} value calculated from the D–R model at different temperatures is in the range of 9.81–11.36 kJ mol^{-1} (>8 kJ mol^{-1}) (Fig. 4d). Therefore, the U(VI) removal process on Fe/P-CN-800 is mainly chemisorption, including chemical reduction and coordination,[45] which is consistent with the adsorption kinetics results.

To gain insight into the removal characteristics of U(VI) on Fe/P-CN-800 at different temperatures, thermodynamic parameters (involving the change in the standard enthalpy (ΔH°, kJ mol^{-1}), entropy (ΔS°, J K^{-1} mol^{-1}) and free energy (ΔG°, kJ mol^{-1})) were employed to liner fit the experimental data (Fig. 4e) according to eqn (S10) and (S11).†[12,51,54] According to Table S4,† the positive ΔH° value (4.29 kJ mol^{-1}) and negative ΔG° value imply an endothermic and spontaneous removal process, respectively. Meanwhile, the more negative ΔG° value at high temperature indicates that higher temperatures are conducive for the removal of U(VI). Also, the positive ΔS° value (62.22 J mol^{-1} K^{-1}) suggests that the active sites coordinate more U(VI) ions and H_2O molecules actively participate in the reaction in aqueous solution, resulting in enhanced randomness at the solid–liquid interface.[55]

Thermal reactivation of Fe/P-CN-800

Reusability and stability are also critical for improving the ecological and economic value of adsorbents. According to Fig. 3a, the U(VI) removal efficiency of Fe/P-CN-800 was reduced at a lower pH, meaning that the loaded uranium would be desorbed by using acid medium. Specifically, about 95.58% U(VI) ions could be removed from the absorbent with 0.2 mol L^{-1} HNO_3 solution (Fig. S5a†). Thus, HNO_3 solution with this concentration was selected as the eluent in the cycling experiment. Specifically, after every cycle, the spent Fe/P-CN-800 loaded with U(VI) was immersed in 0.2 mol L^{-1} HNO_3 solution and stirred for 12 h in air, centrifuged, washed with water repeatedly and freeze-dried for 12 h consecutively (the deposited uranium on Fe/P-CN-800 was desorbed). Afterward, it was calcined at a slow heating rate of 0.1 °C min^{-1} to 300 °C in air, then at 1.5 °C min^{-1} to 800 °C for 2 h under an N_2 atmosphere for the next cycle reaction. Herein, the main purpose of the thermal treatment was to reactivate the Fe nanocrystals in Fe/P-CN-800 for reuse. As depicted in Fig. S5b,† the elution efficiency of uranium from Fe/P-CN-800 was found to be 95.58%, 93.61%, 91.89%, 90.72%, and 88.32% for each cycle in five cycles of reuse, respectively. The removal capacity of U(VI) on Fe/P-CN-800 after five continuous cycles of reuse is displayed in Fig. 4f.

Although the maximum removal capacity of Fe/P-CN-800 was slightly reduced from 306.76 to 269.32 mg g^{-1} after five cycles, it showed excellent reusability. Surprisingly, the Fe^0 nanoparticles could be reactivated by heat treatment for the cyclic reuse process.[56] However, the element content of Fe/P-CN-800 after five continuous cycles of reuse was analysed by EDS, as shown in Fig. S5c,† and the weight proportion of Fe was calculated to be 21.06%, which is lower than that of the fresh Fe/P-CN-800. Therefore, the slightly reduced removal capacity after five cycles can be explained by two aspects. Firstly, some of the Fe^0 nanoparticles were oxidized to the stable valence of Fe^{3+} and dissolved in the elution solution, resulting in a decline in reduction capacity. Then the incompletely desorbed U(VI) ions occupy some of the active sites. In addition, the magnetic separation property (Fig. 4f inset digital image) endows Fe/P-CN-800 convenient separation. These observations demonstrate that Fe/P-CN-800 can be used in a permeable reactive barrier (PRB) system to *in situ* immobilize U(VI) in groundwater.

Mechanism for removal of U(VI)

To further understand the interaction mechanism of U(VI) on Fe/P-CN-800, a systematic investigation including FT-IR, XPS, and element mapping of Fe/P-CN-800 and Fe/P-CN-800-U (after U(VI) uptake) was performed. Compared with the FTIR spectrum Fe/P-CN-800, the new peak located at 978 cm^{-1} for Fe/P-CN-800-U can be ascribed to the asymmetric vibration of the UO_2^{2+}

Table 1 Comparison of Fe/P-CN-800 with other NZVI-based absorbents

Sorbent	Experimental conditions	q_{max} (mg g^{-1})	Ref.
FC-supported Fe	pH = 4.0, $T = 303.15$ K	125.52	46
nZVI/C composites	pH = 4.0, $T = 28.15$ K	186.92	47
LDH@nZVI	pH = 5.0, $T = 283.15$ K	176	48
Fe/N-C	pH = 6.0, $T = 293.15$ K	232.54	23
Fe–PANI–GA	pH = 5.5, $T = 293.15$ K	350.47	49
Nano-Fe + *B. subtilis*	pH = 5.5, $T = 298.15$ K	215.17	50
NZVI/MC800	pH = 4.0, $T = 298.15$ K	203.94	51
Fe–SC	pH = 4.0, $T = 298$ K	89	52
nZVI in the presence of phosphate	pH = 4.0, $T = 298.15$ K	84.03	53
Fe/P-CN-800	pH = 4.5, $T = 298.15$ K	372.60	This work

group (Fig. 5a).[57] The peak at 1340 cm^{-1} can be ascribed to the nitrate stretching modes due to the used uranyl nitrate solution.[58] Therefore, U(VI) was captured on Fe/P-CN-800 successfully. The removal process may be closely related to the functional groups containing oxygen or nitrogen generated from the heterogeneous atoms.

As confirmed by XPS, C, O, N, P, and Fe elements appear in the XPS spectra of both samples and the characteristic peak of U 4f is also observed for Fe/P-CN-800-U (Fig. 5b).[59,60] As shown in Fig. 5c, the U4f spectrum of Fe/P-CN-800-U can be divided into two distinct peaks at 382 eV and 393 eV, corresponding to U 4f$_{7/2}$ and U 4f$_{5/2}$, respectively. Furthermore, these peaks can be fitted to U(VI) (382.4 and 393.5 eV) and U(IV) (381.7 and 392.4 eV) species, respectively, indicating the stable chemical bond between U(VI) with the functional groups on the surface of Fe/P-CN-800 and the reduced U(IV) by the NZVI in the body of Fe/P-CN-800.[20] According to the U4f peak area, the ratio of U(IV) to U(VI) is about 3 : 2, as calculated based on the XPS results. As shown in Fig. 5d, the peaks at 710.8 eV and 725.3 eV can be assigned to Fe 2p$_{3/2}$ and Fe 2p$_{1/2}$ in the Fe^{2+} oxides,[16] respectively, and the peak at 706.9 eV is related to Fe^0.[61] After capture, the broad Fe 2p$_{3/2}$ and Fe 2p$_{1/2}$ peaks at 712.8 and 726.5 eV, respectively, can be identified as Fe^{3+} oxides.[62] The existence of Fe^{3+} and the disappearance of Fe^0 strongly support the explanation that Fe^{2+} and Fe^0 can both reduce U(VI) and to U(IV),[63] and the reduction process is as follows.

$$2Fe^0 + 3UO_2^{2+} \rightarrow 3UO_2 + 2Fe^{3+} \quad (1)$$

$$Fe^0 + UO_2^{2+} \rightarrow UO_2 + 2Fe^{2+} \quad (2)$$

$$2Fe^{2+} + UO_2^{2+} \rightarrow UO_2 + 2Fe^{3+} \quad (3)$$

As presented in Fig. 5e, the P 2p spectrum of Fe/P-CN-800 could be fitted by P–O and P–C at 133.6 and 132.7 eV, respectively. Notably, the P–O peak located at 133.6 eV in Fe/P-CN-800-U is a broad band with a reduced relative intensity, indicating the enhanced electron density of P atoms due to the generation of new chemical bonds with U(VI).[44] Additionally, four types of nitrogen groups, namely pyridinic N, pyrrolic N, graphitic N and oxidized species at 398.3, 398.9, 400.1 and 401.1 eV appeared in the N 1s spectrum (Fig. 5f), respectively.[64] For Fe/P-CN-800-U, the intensity of the oxidized N peak decreased, and even disappeared, while the pyrrolic N and pyridinic N peaks obviously shifted to lower binding energies at 398.4 and 397.7 eV, respectively. These changes indicate that the nitrogen functional groups can act as active sites to chelate with U(VI) ions, leading to a change in the distribution of electrons in the surrounding environment.[65]

In addition, the major peaks at 529.9 eV, 530.9 eV, 531.4 eV, 532.2 eV and 533.2 eV in the O 1s spectra correspond to Fe–O, C=O, P=O, C–O and N–O bonds, respectively (Fig. S6a†).[66] However, they shifted to the lower binding energies of 529.7 eV, 530.6 eV, 531.5 eV, 531.9 and 532.9 eV, respectively, after adsorbing U(VI). The obviously weakened intensity and shifted binding energy demonstrate the formation of covalent bonds between the oxygen and uranium atoms. The new peak at 534.3 eV corresponds to adsorbed water. As depicted in Fig. S6b,† the C 1s spectrum of Fe/P-CN-800 can be fitted to four main peaks associated with C–C/C–N (284.5 eV), C–P (285.2 eV), C=N (286.4 eV), and O–C=O (288.4 eV).[67] The O–C=O peak intensity slight decreased, meanwhile the peaks for C–P and C=N shifted to lower binding energies after adsorbing U(VI) due to the aggregation of U(VI) by these functional groups. Additionally, the SEM-mapping images show that C, O, N, P, Fe and U elements were uniformly distributed on Fe/P-CN-800 (Fig. S7†).

Finally, the removal mechanism between U(VI) and Fe/P-CN-800 is elucidated and postulated in Scheme 2. On the one hand, benefiting from its negatively charged surface, porous structure and abundant active sites, U(VI) ions can be attracted to and enter Fe/P-CN-800 by electrostatic interaction and intraparticle

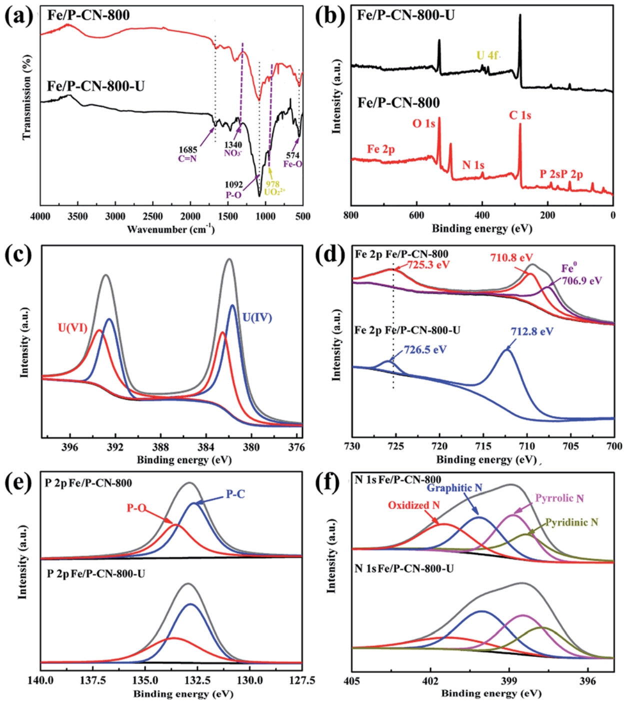

Fig. 5 (a) FT-IR spectra and (b) XPS spectra of Fe/P-CN-800 and Fe/P-CN-800-U. XPS patterns of (c) U 4f for Fe/P-CN-800-U, (d) Fe 2p, (e) P 2p and (f) N 1 s.

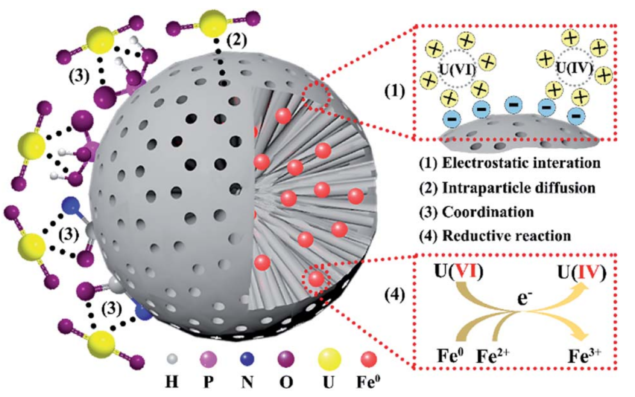

Scheme 2 Removal mechanisms of Fe/P-CN-800 with U(VI) sorption.

diffusion, respectively. Then, a strong coordination interaction is formed between the functional groups and U(VI), resulting in an enhanced removal capacity. On the other hand, the solvable U(VI) can be reduced to insoluble U(IV) by Fe^0 nanoparticles or Fe^{2+} of Fe/P-CN-800 according to the chemical reduction interaction, which simultaneously enhances the U(VI) removal performance through solid–liquid separation. Therefore, the removal capacity of Fe/P-CN-800 for U(VI) is attributed to the synergistic mechanism combining adsorption and reductive reaction in the natural environment.

Conclusions

In summary, we presented a promising method to remove U(VI) using N and P co-doped magnetic carbon spheres encapsulating well-dispersed active Fe nanocrystals (Fe/P-CN), which were fabricated *via* a simple copolymer pyrolysis strategy at different temperatures. The systematic characterization demonstrated that Fe/P-CN-800 possesses a stable spherical structure, abundant binding groups and Fe^0 nanocrystals. As an effective adsorbent, Fe/P-CN-800 exhibited a high U(VI) removal efficiency of 306.76 mg g^{-1} at 300 min and could be easily magnetic separated from aqueous solution. In particular, the removal capacity was maintained at almost 90% of the initial value after five cycles of reuse. The spent Fe/P-CN-800 could be reactivated *via* simple heat treatment. In addition, the removal mechanism of U(VI) was systematically elucidated to be the synergistic effect of adsorption and the reductive reaction. Based on these findings, this work significantly evidences the potential practical applications of this type of co-doped magnetic porous carbon in the field of environmental remediation.

Conflicts of interest

The authors declare no competing financial interest.

Acknowledgements

This work was financially supported by the National Natural Science Foundation of China (21561002, 21866004, 21866003), the Jiangxi Provincial Department of Science and Technology (Grant No. 2018ACB21007), the Major Discipline Academic and Technical Leaders Training Program of Jiangxi Province (Grant No. 20182BCB22011) and the Education Department of Jiangxi Provincial (Grant No. GJJ171515).

References

1 K. M. Campbell, T. J. Gallegos and E. R. Landa, Biogeochemical aspects of uranium mineralization, mining, milling, and remediation, *Appl. Geochem.*, 2015, **57**, 206–235.

2 B. Ahmed, B. Cao, B. Mishra, M. I. Boyanov, K. M. Kemner, J. K. Fredrickson and H. Beyenal, Immobilization of U(VI) from oxic groundwater by hanford 300 area sediments and effects of columbia river water, *Water Res.*, 2012, **46**, 3989–3998.

3 M. Gavrilescu, L. V. Pavel and I. Cretescu, Characterization and remediation of soils contaminated with uranium, *J. Hazard. Mater.*, 2009, **163**, 475–510.

4 Y. Xie, C. L. Chen, X. M. Ren, X. X. Wang, H. Y. Wang and X. K. Wang, Emerging natural and tailored materials for uranium-contaminated water treatment and environmental remediation, *Prog. Mater. Sci.*, 2019, **103**, 180–234.

5 E. Schnug and B. G. Lottermoser, Fertilizer-Derived Uranium and its Threat to Human Health, *Environ. Sci. Technol.*, 2013, **47**, 2433–2434.

6 Y. L. Wang, Z. Y. Liu, Y. X. Li, Z. L. Bai, W. Liu, Y. X. Wang, X. M. Xu, C. L. Xiao, D. P. Sheng, J. Diwu, J. Su, Z. F. Chai, A. S. Thoma and S. A. Wang, Umbellate distortions of the uranyl coordination environment result in a stable and porous polycatenated framework that can effectively remove cesium from aqueous solutions, *J. Am. Chem. Soc.*, 2015, **137**, 6144–6147.

7 S. J. Yu, X. X. Wang, Y. F. Liu, Z. S. Chen, Y. H. Wu, Y. Liu, H. W. Pang, G. Song, J. R. Chen and X. K. Wang, Efficient removal of uranium(VI) by layered double hydroxides supported nanoscale zero-valent iron: a combined experimental and spectroscopic studies, *Chem. Eng. J.*, 2019, **365**, 51–59.

8 M. Ahmad, J. Q. Wang, Z. T. Yang, Q. Y. Zhang and B. L. Zhang, Ultrasonic-assisted preparation of amidoxime functionalized silica framework via oil-water emulsion method for selective uranium adsorption, *Chem. Eng. J.*, 2020, **389**, 124441.

9 Z. B. Zhang, C. Liu, Z. M. Dong, Y. Dai, G. X. Xiong, Y. H. Liu, Y. Q. Wang, Y. C. Wang and Y. H. Liu, Synthesis of flower-like MoS_2/g-C_3N_4 nanosheet heterojunctions with enhanced photocatalytic reduction activity of uranium(VI), *Appl. Surf. Sci.*, 2020, **520**, 146352.

10 D. H. Phillips, T. Van Nooten, L. Bastiaens, M. I. Russell, K. Dickson, S. Plant, J. M. E. Ahad, T. Newton, T. Elliot and R. M. Kalin, Ten years performance evaluation of a field-scale zero-valent iron permeable reactive barrier installed to remediate trichloroethene contaminated groundwater, *Environ. Sci. Technol.*, 2010, **44**, 3861–3869.

11 S. Tsarev, R. N. Collins, E. S. Ilton, A. Fahy and T. D. Waite, The short-term reduction of uranium by nanoscale zero-valent iron (nZVI): role of oxide shell, reduction mechanism and the formation of U(V)-carbonate phases, *Environ. Sci.: Nano*, 2017, **4**, 1304–1313.

12 Y. Shin, S. Bae and W. Lee, Formation of surface mediated iron colloids during U(VI) and nZVI interaction, *Adv. Environ. Res.*, 2013, **2**, 167–177.

13 J. Duan, H. D. Ji, W. Liu, X. Zhao, B. Han, S. T. Tian and D. Y. Zhao, Enhanced immobilization of U(VI) using a new type of FeS-modified Fe^0 core-shell particles, *Chem. Eng. J.*, 2019, **359**, 1617–1628.

14 X. Y. Wang, P. Wang, J. Ma, H. L. Liu and P. Ning, Synthesis, characterization, and reactivity of cellulose modified nano zero-valent iron for dye discoloration, *Appl. Surf. Sci.*, 2015, **345**, 57–66.

15 X. Q. Zhao, X. M. Dou, D. Mohan, C. U. Pittman Jr, Y. S. Ok and X. Jin, Antimonate and antimonite adsorption by

a polyvinyl alcoholstabilized granular adsorbent containing nanoscale zero-valent iron, *Chem. Eng. J.*, 2014, **247**, 250–257.

16 Y. T. Wei, S. C. Wu, S. W. Yang, C. H. Che, H. L. Lien and D. H. Huang, Biodegradable surfactant stabilized nanoscale zero-valent iron for in situ treatment of vinyl chloride and 1,2-dichloroethane, *J. Hazard. Mater.*, 2012, **211**, 373–380.

17 Y. M. Li, W. Cheng, G. D. Sheng, J. F. Li, H. P. Dong, Y. Chen and L. Z. Zhu, Synergetic effect of a pillared bentonite support on Se(VI) removal by nanoscale zero valent iron, *Appl. Catal., B*, 2015, **174–175**, 329–335.

18 N. Yuan, G. K. Zhang, S. Guo and Z. Wan, Enhanced ultrasoundassisted degradation of methyl orange and metronidazole by rectoritesupported nanoscale zero-valent iron, *Ultrason. Sonochem.*, 2016, **28**, 62–68.

19 S. Bhowmick, S. Chakraborty, P. Mondal, W. V. Renterghem, S. V. D. Berghe, G. R. Ross, D. Chatterjee and I. M. glesias, Montmorillonite-supported nanoscale zero-valent iron for removal of arsenic from aqueous solution: kinetics and mechanism, *Chem. Eng. J.*, 2014, **243**, 14–23.

20 J. N. Xiao, B. Y. Gao, Q. Y. Yue, Y. Y. Sun, J. J. Kong, Y. Gao and Q. Li, Characterization of nanoscale zero-valent iron supported on granular activated carbon and its application in removal of acrylonitrile from aqueous solution, *J. Taiwan Inst. Chem. Eng.*, 2015, **55**, 152–158.

21 G. D. Sheng, A. Alsaedi, W. Shammakh, S. Monaquel, J. Sheng, X. K. Wang, H. Li and Y. Y. Huang, Enhanced sequestration of selenite in water by nanoscale zero valent iron immobilization on carbon nanotubes by a combined batch, XPS and XAFS investigation, *Carbon*, 2016, **99**, 123–130.

22 U. N. Maiti, W. J. Lee, J. M. Lee, Y. Oh, J. Y. Kim, J. E. Kim, J. Shim, T. H. Han and S. O. Kim, 25th anniversary article: chemically modified/doped carbon nanotubes & graphene for optimized nanostructures & nanodevices, *Adv. Mater.*, 2014, **26**, 40–66.

23 K. R. Zhu, C. L. Chen, M. W. H. Xu, K. Chen, X. L. Tan, M. Wakeel and N. S. Alharbi, In situ carbothermal reduction synthesis of Fe nanocrystals embedded into N-doped carbon nanospheres for highly efficient U(VI) adsorption and reduction, *Chem. Eng. J.*, 2018, **331**, 395–405.

24 Y. S. L. Yang, L. Peng, P. P. Huang, X. S. Wang, Y. B. Sun, C. Y. Cao and W. G. Song, Nitrogen, phosphorus, and sulfur co-doped hollow carbon shell as superior metal-free catalyst for selective oxidation of aromatic alkanes, *Angew. Chem.*, 2016, **128**, 4084–4088.

25 V. S. Kale, H. Minsik, C. Hogeun, K. Jeongmin, C. S. J. Youngmoo, J. Yang, J. H. Kim, Y. J. Ko, Y. Z. Piao and T. Hyeon, Microporosity-controlled synthesis of heteroatom codoped carbon nanocages by wrap-bake-sublime approach for flexible all-solid-state-supercapacitors, *Adv. Funct. Mater.*, 2018, **28**, 1803786.

26 W. Zhang, A. Bu, Q. Y. Ji, L. F. Min, S. Zhao, Y. X. Wang and J. Chen, pKa-Directed incorporation of phosphonates into MOF-808 via ligand exchange: stability and adsorption properties for uranium, *ACS Appl. Mater. Interfaces*, 2019, **37**, 33931–33940.

27 L. C. Yang, Y. Shi, Q. S. Gao, B. Wang, Y. P. Wu and Y. Tang, The production of carbon nanospheres by the pyrolysis of polyacrylonitrile, *Carbon*, 2008, **46**, 1816–1818.

28 G. Z. Yang, B. B. Yu, S. Song, Z. H. Tang, D. G. Yu and J. H. Yang, Preparation and dispersity of carbon nanospheres by carbonizing polyacrylonitrile microspheres, *RSC Adv.*, 2017, **7**, 16341–16347.

29 M. Bellardita, E. I. García-López, G. Marcì, I. Krivtsov, J. R. García and L. Palmisano, Selective photocatalytic oxidation of aromatic alcohols in water by using P doped g-C_3N_4, *Appl. Catal. B Environ.*, 2018, **220**, 222–233.

30 Y. G. Xu, F. Y. Ge, Z. G. Chen, S. Q. Huang, W. Wei, M. Xie, H. Xu and H. M. Li, One-step synthesis of Fe-doped surface-alkalinized g-C_3N_4 and their improved visible-light photocatalytic performance, *Appl. Surf. Sci.*, 2019, **469**, 739–746.

31 J. A. Zhang, R. Yuan, S. Natesakhawat, Z. Y. Wang, Y. P. Zhao, J. J. Yan, S. Y. Liu, J. Lee, D. L. Luo, E. Gottlieb, T. Kowalewski, M. R. Bockstaller and K. Matyjaszewski, Individual nanoporous carbon spheres with high nitrogen content from polyacrylonitrile nanoparticles with sacrificial protective layers, *ACS Appl. Mater. Interfaces*, 2017, **43**, 37804–37812.

32 F. Q. Ma, B. R. Dong, Y. Y. Gui, M. Cao, L. Han, C. S. Jiao, H. T. Lv, J. J. Hou and Y. Xue, Adsorption of low-concentration uranyl ion by amidoxime polyacrylonitrile fibers, *Ind. Eng. Chem. Res.*, 2018, **57**, 17384–17393.

33 Y. W. Cai, C. F. Wu, Z. Y. Liu, L. J. Zhang, L. H. Chen, J. Q. Wang, X. K. Wang, S. T. Yang and S. A. Wang, Fabrication of phosphorylated graphene oxide-chitosan composite for highly effective and selective capture of U(VI), *Environ. Sci.: Nano*, 2017, **4**, 1876–1886.

34 C. C. Ding, W. C. Cheng, X. Q. Nie and F. C. Yi, Synergistic mechanism of U(VI) sequestration by magnetite-graphene oxide composites: Evidence from spectroscopic and theoretical calculation, *Chem. Eng. J.*, 2017, **324**, 113–121.

35 Q. H. Liang, Z. Li, X. L. Yu, Z. H. Huang, F. Y. Kang and Q. H. Yang, Macroscopic 3D porous graphitic carbon nitride monolith for enhanced photocatalytic hydrogen Evolution, *Adv. Mater.*, 2015, **27**, 4634–4639.

36 Q. Zhang, D. L. Zhao, S. J. Feng, Y. Y. Wang, J. Jin, A. Alsaedi, T. Hayat and C. L. Chen, Synthesis of nanoscale zero-valent iron loaded chitosan for synergistically enhanced removal of U(VI) based on adsorption and reduction, *J. Colloid Interface Sci.*, 2019, **5**, 735–743.

37 X. J. Guo, R. R. Chen, Q. Liu, J. Y. Liu, H. S. Zhang, J. Yu, M. L. Zhang and J. Wang, Superhydrophilic phosphate and amide functionalized magnetic adsorbent: a new combination of anti-biofouling and uranium extraction from seawater, *Environ. Sci.: Nano*, 2018, **5**, 2346–2356.

38 W. C. Cheng, C. C. Ding, Q. Y. Wu, X. X. Wang, Y. B. Sun, W. Q. Shi, T. Hayat, A. Alsaedi, Z. F. Chai and X. K. Wang, Mutual effect of U(VI) and Sr(II) with graphene oxides: evidence from EXAFS and theoretical calculations, *Environ. Sci.: Nano*, 2017, **4**, 1124–1131.

39 S. Zhang, X. S. Zhao, B. Li, C. Y. Bai, Y. Li, L. Wang, R. Wen, M. C. Zhang, L. J. Ma and S. J. Li, “Stereoscopic” 2D super-

microporous phosphazene-based covalent organic framework: design, synthesis and selective sorption towards uranium at high acidic condition, *J. Hazard. Mater.*, 2016, **314**, 95–104.

40 I. Pidchenko, K. O. Kvashnina, T. Yokosawa, N. Finck, S. Bahl, D. Schild, R. Polly, E. Bohnert, A. Rossberg, J. Göttlicher, K. Dardenne, J. Rothe, T. Schäfer, H. Geckeis and T. Vitova, Uranium redox transformations after U(VI) coprecipitation with magnetite nanoparticles, *Environ. Sci. Technol.*, 2017, **51**, 2217–2225.

41 W. Zhang, G. Ye and J. Chen, New insights into the uranium adsorption behavior of mesoporous SBA-15 silicas decorated with alkylphosphine oxide ligands, *RSC Adv.*, 2016, **6**, 1210–1217.

42 D. Li, S. Egodawatte, D. I. Kaplan, S. C. Larsen, S. M. Serkiz, J. C. Seaman, K. G. Scheckel, J. Lin and Y. M. Pan, Sequestration of U(VI) from acidic, alkaline, and high ionic-strength aqueous media by nationalized magnetic mesoporous silica nanoparticles: capacity and binding mechanisms, *Environ. Sci. Technol.*, 2017, **51**, 14330–14341.

43 I. C. Popescu, P. Filip, D. Humelnicu, I. Humelnicu, T. B. Scott and R. A. Crane, Removal of uranium (VI) from aqueous systems by nanoscale zero-valent iron particles suspended in carboxy-methyl cellulose, *J. Nucl. Mater.*, 2013, **443**, 250–255.

44 Z. B. Zhang, Z. M. Dong, X. X. Wang, Y. Dai, X. H. Cao, Y. Q. Wang, R. Hua, H. T. Feng, J. R. Chen, Y. H. Liu, B. W. Hu and X. K. Wang, Synthesis of ultralight phosphorylated carbon aerogel for efficient removal of U(VI): batch and fixed-bed column studies, *Chem. Eng. J.*, 2019, **370**, 1376–1387.

45 K. Vijayaraghavan, T. V. N. Padmesh, K. Palanivelu and M. Velan, Biosorption of nickel(II) ions onto Sargassum wightii: application of two-parameter and three-parameter isotherm models, *J. Hazard. Mater.*, 2006, **133**, 304–308.

46 L. J. Kong, H. M. Zhang, K. M. Shi, M. H. Su, Z. H. Diao, J. Y. Long, L. A. Hou, G. Song and D. Y. Chen, Synthesis of FC-supported Fe through a carbothermal process for immobilizing uranium, *J. Hazard. Mater.*, 2018, **357**, 168–174.

47 H. B. Liu, M. X. Li, T. H. Chen, C. L. Chen, S. Alharbi, T. Hayat, D. Chen, Q. Zhang and Y. B. Sun, New Synthesis of nZVI/C composites as an efficient adsorbent for the uptake of U(VI) from aqueous solutions, *Environ. Sci. Technol.*, 2017, **51**, 9227–9234.

48 Y. Y. Dong, Z. M. Dong, Z. B. Zhang, Y. H. Liu, W. W. Cheng, H. Miao, X. X. He and Y. Xu, A POM constructed from super-sodalite cage with extra-large 24-membered channels: As effective sorbent for uanium adsorption, *ACS Appl. Mater. Interfaces*, 2017, **9**, 22088–22092.

49 L. L. Chen, S. J. Feng, D. L. Zhao, S. H. Chen, F. F. Li and C. L. Chen, Efficient sorption and reduction of U(VI) on zero-valent iron -polyaniline-graphene aerogel ternary composite, *J. Colloid Interface Sci.*, 2016, **490**, 197–206.

50 C. C. Ding, W. C. Cheng, Y. B. Sun and X. K. Wang, Effects of bacillus subtilis on the reduction of U(VI) by nano-Fe^0, *Geochim. Cosmochim. Acta*, 2015, **165**, 86–107.

51 Z. M. Lv, S. M. Yang, L. Chen, A. Alsaedi, T. Hayat and C. L. Chen, Nanoscale zerovalent iron/magnetite carbon composites for high efficient immobilization of U(VI), *J. Environ. Sci.*, 2019, **76**, 377–387.

52 M. Q. Qiu, M. Wang, Q. Z. Zhao, B. W. Hu and Y. L. Zhu, XANES and EXAFS investigation of uranium incorporation on nZVI in the presence of phosphate, *Chemosphere*, 2018, **201**, 764–771.

53 L. J. Kong, Y. T. Zhu, M. Wang, Z. X. Li, Z. C. Tan, R. B. Xu, H. M. Tang, X. Y. Chang, Y. Xiong and D. Y. Chen, Simultaneous reduction and adsorption for immobilization of uranium from aqueous solution by nano-flake Fe-SC, *J. Hazard. Mater.*, 2016, **320**, 435–441.

54 E. C. Lima, A. Hosseini-Bandegharaei, J. C. Moreno-Piraján and I. Anastopoulos, A critical review of the estimation of the thermodynamic parameters on adsorption equilibria. Wrong use of equilibrium constant in the Van't Hoof equation for calculation of thermodynamic parameters of adsorption, *J. Mol. Liq.*, 2019, **273**, 425–434.

55 Y. D. Zou, X. X. Wang, Y. J. Ai, Y. H. Liu, Y. F. Ji, H. Q. Wang, T. Hayat, A. Alsaedi, W. P. Hu and X. K. Wang, b-Cyclodextrin modified graphitic carbon nitride for the removal of pollutants from aqueous solution: experimental and theoretical calculation study, *J. Mater. Chem. A*, 2016, **37**, 14170–14179.

56 H. Park, A. May, L. Portilla, H. Dietrich, F. Münch, T. Rejek, M. Sarcletti, L. Banspach, D. Zahn and M. Halik, Magnetite nanoparticles as efficient materials for removal of glyphosate from water, *Nature Sustainability*, 2020, **3**, 129–135.

57 Z. M. Dong, Z. B. Zhang, R. Z. Zhou, Y. Y. Dong, Y. Dai, X. H. Cao, Y. Q. Wang and Y. H. Li, Construction of oxidized millimeter-sized hierarchically porous carbon spheres for U(VI) adsorption, *Chem. Eng. J.*, 2020, **386**, 123944.

58 J. Huynh, R. Palacio, F. Safizadeh, G. Lefèvre, M. Descostes, L. Eloy, N. Guignard, J. Rousseau, S. Royer, E. Tertre and I. Batonneau-Gener, Uranium in water adsorption over NH_2 functionalized ordered silica, *ACS Appl. Mater. Interfaces*, 2017, **18**, 15672–15684.

59 Y. P. Wang, Q. Fu, C. Li, H. H. Li and H. Tang, Nitrogen and phosphorous dual-doped graphene aerogel confined monodisperse iron phosphide nanodots as an ultrafast and long-term cycling anode material for sodium-ion batteries, *ACS Sustainable Chem. Eng.*, 2018, **11**, 15083–15091.

60 T. Wen, J. Wang, S. J. Yu, Z. S. Chen, T. Hayat and X. K. Wang, Magnetic porous carbonaceous material produced from tea waste for efficient removal of As(V), Cr(VI), humic Acid, and dyes, *ACS Sustainable Chem. Eng.*, 2017, **5**, 4371–4380.

61 H. C. Tao, L. Y. Xiong, S. L. Du, Y. Q. Zhang, X. L. Yang and L. L. Zhang, Interwoven N and P dual-doped hollow carbon fibers/graphitic carbon nitride: An ultrahigh capacity and rate anode for Li and Na ion batteries, *Carbon*, 2017, **122**, 54–63.

62 Y. M. Zhang, H. S. Zhang, Q. Liu, R. R. Chen, J. Y. Liu, J. Yu, X. Y. Jing, M. L. Zhang and J. Wang, Polypyrrole modified Fe^0-loaded graphene oxide for the enrichment of uranium (VI) from simulated seawater, *Dalton Trans.*, 2018, **471**, 12984–12992.

63 Y. H. Cao, J. N. Huang, Y. H. Li, S. Qiu, J. R. Liu, A. Khasanov, M. A. Khan, D. P. Young, F. Peng, D. P. Cao, X. F. Peng and K. L. Hong, One-pot melamine derived nitrogen dopedmagnetic carbon nanoadsorbents with enhanced chromium removal, *Carbon*, 2016, **109**, 640–649.

64 M. Majumder, B. R. Choudhary and A. K. Thakur, Hemispherical nitrogen-doped carbon spheres integrated with polyindole as high performance electrode material for supercapacitor applications, *Carbon*, 2019, **142**, 650–661.

65 F. Q. Lin, Y. H. Wang and Z. Lin, One-pot synthesis of nitrogen-enriched carbon spheres for hexavalent chromium removal from aqueous solution, *RSC Adv.*, 2016, **6**, 33055–33062.

66 Z. J. Li, L. Wang, L. Y. Yuan, C. L. Xiao, L. Mei, L. R. Zheng, J. Zhang, J. H Yang, Y. L. Zhao, Z. T. Zhu, Z. F. Chai and W. Q. Shi, Efficient removal of uranium from aqueous solution by zero-valent iron nanoparticle and its graphene composite, *J. Hazard. Mater.*, 2015, **290**, 26–33.

67 W. Wang, J. M. Li, Y. M. Kang, F. X. Wang, J. N. Song and Z. Q. Lei, Facile and scalable preparation of nitrogen, phosphorus codoped nanoporous carbon as oxygen reduction reaction electrocatalyst, *Electrochim. Acta*, 2017, **248**, 11–19.